Raman source using a hollow-core fiber for ozone monitoring in the lower troposphere

Joris Weinzaepflen[1,2,3], François Ravetta[1], Stéphane Victori[2], Gérard Ancellet[1], Cristelle Cailteau-Fischbach[1,4], Vincent Mariage[1], Frédéric Delahaye[5], Frédéric Gérôme[5,6], and Fetah Benabid[5,6]

[1]Laboratoire Atmosphères et Observations Spatiales (LATMOS) / Institut Pierre-Simon Laplace (IPSL), Sorbonne Université, Université Versailles Saint-Quentin, CNRS, 4 place Jussieu 75252 Paris, France
[2]CIMEL Electronique, 172 rue de Charonne - 75011 Paris, France
[3]Université Paris-Saclay, Institut d'Optique Graduate School, CNRS, Laboratoire Charles Fabry, 2 Av. Augustin Fresnel 91127 Palaiseau, France
[4]Sorbonne Université, CNRS, UAR OMA Terra, Observatoire des Sciences de l'Univers Ecce Terra, Paris Cedex 5, France
[5]GLOphotonics, 123 Avenue Albert Thomas, Limoges 87060, France
[6]GPPMM Group Xlim, 123 Avenue Albert Thomas Limoges, 87060, France

Correspondence: Joris Weinzaepflen (j-weinzaepflen@cimel.fr)

Abstract. ~~The~~ This paper presents the integration and first atmospheric deployment of a deuterium-filled hollow-core fiber (HCF) Raman source in the DIfferential Absorption microlidar for Boundary Layer Ozone (DIABLO) ~~is designed for boundary-layer~~ prototype. The objective is to assess the feasibility of this low-pulse-energy transmitter architecture for planetary boundary layer ozone profiling. This ~~instrument uses a~~ approach aims to support further reductions in instrument size and cost, complementing existing autonomous ozone lidar capabilities. A diode-pumped, passively Q-switched Nd:YAG laser at 266 nm ~~, coupled to a deuterium-filled hollow-core fiber (HCF)~~ is coupled to the HCF to generate the 289 nm Stokes wavelength ~~via~~ through stimulated Raman scattering~~(SRS)~~. The high Raman gain ~~in the gas-filled HCF~~ enables efficient UV conversion ~~with significantly lower pump energy than required in traditional~~ at substantially lower pump energies than conventional free-space Raman cells. At the ~~output of the fiber~~ fiber output, 1-ns pulses of approximately 10 μJ at 266 nm and 7 μJ at 289 nm are obtained ~~with~~ at a repetition rate of 1 kHz. ~~First~~ Initial atmospheric measurements in central Paris ~~provide ozone concentrations between~~ yield ozone profiles between approximately 400 ~~m~~ and 1700 m above ground level. These results demonstrate the feasibility of integrating an HCF Raman source into a compact ozone DIAL instrument. Further characterization of transmitter stability and independant validation of ozone vertical profiles are still required to assess the suitability of this prototype for continuous autonomous operation and its accuracy. ~~In contrast with existing UV DIAL ozone systems, which are typically bulky, complex, and operated in campaign-based research configurations, DIABLO targets a compact and low-energy architecture optimized for autonomous boundary-layer monitoring.~~

1 Introduction

Monitoring ozone (O_3) in the lower troposphere is crucial for understanding atmospheric chemistry, assessing air quality, and evaluating its impacts on human health and ecosystems (Monks et al., 2015). Over the past decades, numerous field campaigns have investigated tropospheric ozone variability in polluted environments using a combination of airborne in situ measurements, ozonesondes, and remote sensing observations (Vautard et al., 2003; Ryerson et al., 2013).

Among the remote sensing techniques deployed during these campaigns, ~~lidar~~ LIght Detection And Ranging (lidar) systems play a key role by providing vertically resolved measurements of atmospheric composition. ~~Lidar (Light Detection and Ranging) is an active technique based on the emission of laser pulses and the detection of the backscattered signal from the atmosphere.~~ In particular, ~~Differential Absorption Lidar (DIAL) enables the retrieval of trace gas~~ ozone DIAL retrieves ozone concentration profiles by exploiting the ~~differential~~ difference in ozone absorption between two ~~closely spaced~~ wavelengths (Pelon and Mégie, 1982).

In Europe, major experiments such as ESQUIF ("Etude et Simulation de la Qualité de l'air en Île-de-France") in the Paris region (Vautard et al., 2003) and ESCOMPTE ("Expérience sur Site pour COntraindre les Modèles de Pollution atmosphérique et de Transport d'Emissions") in southern France (Drobinski et al., 2007) highlighted the respective roles of local photochemical production, regional transport, and mesoscale dynamical processes in shaping ~~ozone distributions~~the spatial distribution and vertical structure of ozone. In North America, large-scale campaigns including the Texas Air Quality Study (TexAQS) in 2000 and 2006 (Daum et al., 2004; Senff et al., 2010), the California Research at the Nexus of Air Quality and Climate Change (CalNex) in 2010, the California Baseline Ozone Transport Study (CABOTS) in 2016, the Las Vegas Ozone Study (LVOS) in 2016 and 2017 (Ryerson et al., 2013; Faloona et al., 2020; Langford et al., 2022), the Long Island Sound Tropospheric Ozone Study (LISTOS) in 2018 and 2019 (Couillard et al., 2021), and the TRacking Aerosol Convection ExpeRiment – Air Quality (TRACER-AQ) in 2021 (Liu et al., 2023) have similarly documented the complexity of ozone pollution episodes in urban and coastal environments. In Asia, ozone lidar observations have been conducted through regional campaigns and long-term programs, particularly in Japan and China. In Japan, tropospheric ozone DIAL systems operated by the National Institute for Environmental Studies and the Meteorological Research Institute have been widely used to investigate vertical ozone distribution and long-range transport, notably during the Saga 2015 campaign (Uchino et al., 2017). In China, recent developments have enabled ozone lidar deployments in urban environments to study ~~boundary-layer~~ PBL structure and pollution processes (Su et al., 2017; Wang et al., 2021). These studies consistently emphasized the key role of ~~boundary-layer~~ PBL dynamics—such as vertical mixing, residual layers, and entrainment processes—in controlling both the vertical structure of ozone and its surface concentrations.

~~Differential Absorption Lidar (DIAL) systems have played a central role in documenting the vertical distribution of tropospheric ozone. Both airborne and ground-based UV DIAL instruments have demonstrated the capability to resolve fine-scale ozone structures associated with photochemical production, transport, and boundary-layer evolution, including the influence of mesoscale dynamics (Ancellet and Ravetta , 1998, 2005). In North America, the development of coordinated observational frameworks such as the Tropospheric Ozone Lidar Network (TOLNet) has further advanced the use of DIAL systems for high-temporal-resolution~~

monitoring of boundary-layer ozone. Instruments such as the TROPospheric OZone lidar (TROPOZ), the Tunable Optical Profiler for Aerosol and oZone lidar (TOPAZ), and the Langley Mobile Ozone Lidar (LMOL) provide vertically resolved ozone profiles with temporal resolutions from minutes to hours, enabling detailed investigations of urban pollution processes (Wang et al., 2017). In parallel, long-term observations within networks such as NDACC (Network for the Detection for Atmospheric Composition Change) have demonstrated the capability of ground-based DIAL systems to provide continuous ozone profiling for climatological studies and satellite validation (Leblanc et al., 2016b).

Together, these developments have established UV DIAL lidar as a reference technique for resolving ozone variability in the planetary boundary layer, thanks to its high vertical and temporal resolution. However, despite these capabilities, most existing systems remain complex, bulky, and resource-intensive, restricting their deployment to fixed observatories or dedicated field campaigns. This limitation has motivated recent efforts toward more compact and mobile systems, including reduced-scale lidar architectures. While such developments represent important progress toward operational deployment, they remain largely confined to research applications and do not yet fully meet the requirements for dense, autonomous air-quality monitoring networks.

Satellite observations have also been explored for monitoring ozone in the lower troposphere. Cuesta et al. (2013), and Boynard et al. (2018) demonstrated that combining IASI thermal-infrared measurements with GOME-2 ultraviolet observations increases sensitivity to ozone near the surface and enables the retrieval of lower-tropospheric ozone regional streamers over Europe. However, current satellite products typically provide vertical resolutions of about 1 to 3 km in the lower troposphere and revisit times ranging from several hours to one day, depending on the instrument and retrieval method. These characteristics remain insufficient to capture the fine-scale vertical structure and rapid temporal variability of ozone in the PBL, underscoring the need for continuous, high-resolution ground-based profiling(Ancellet et al., 2022).

Although recent developments Ground-based observations have documented the temporal evolution of ozone vertical structure in the urban boundary layer, including nocturnal transport events in the Baltimore–Washington region (Sullivan et al., 2017), ozone layering during LISTOS (Couillard et al., 2021), and day-to-day variability during the Paris ACROSS campaign (Ancellet et al., 2024). Airborne ozone lidar observations during TexAQS 2006 demonstrated that compact, automated DIAL systems suitable for aircraft deployment can provide ozone measurements in the lower troposphere (Senff et al., 2010). Networks such as the Tropospheric Ozone Lidar Network (TOLNet) and the Network for the Detection of Atmospheric Composition Change (NDACC) provide coordinated observations for atmospheric research, satellite validation and model evaluation (Wang et al., 2017). Extended autonomous ozone profiling has also been demonstrated. The Autonomous Mobile Ozone Lidar Instrument for Tropospheric Experiments (AMOLITE) provides near-continuous observations except during precipitation (Strawbridge et al., 2018). More recently, the Small Mobile Ozone Lidar (SMOL) (Chouza et al., 2025) demonstrate that compact mobile ozone DIAL systems are feasible, truly small-scale microlidars suitable for daily PBL monitoring remain scarce. There is therefore a need for instruments combining high-resolution PBL profiling capabilities with reduced size, lower power consumption, and simplified operation compatible with continuous, long-term monitoring. was developed for autonomous operation with limited maintenance, including measurement schedules extending to 24/7 operation (Chouza et al., 2025). These developments demonstrate that ozone lidar observations are not restricted to short, operator-dependent measurement periods. Nevertheless,

further reductions in instrument size, energy requirements and cost remain relevant for wider deployment. Many existing systems require substantial optical, mechanical and environmental-control infrastructure. Even SMOL, which was specifically designed to improve affordability and portability, has dimensions of approximately $1 \times 1.5 \times 2$ m and a mass of approximately 400 kg (Chouza et al., 2025). These considerations motivate the investigation of alternative transmitter architectures requiring lower pulse energies and smaller wavelength-conversion modules.

A key technological challenge in miniaturizing ozone DIAL systems lies in the generation of suitable ultraviolet (UV) wavelength pairs with a good trade-off between pulse energy and repetition rate for optimal signal-to-noise ratio in the lowermost troposphere and safe unattended operation in air quality monitoring network. Traditionally, Raman wavelength conversion for ozone DIAL has relied on free-space Raman cells filled with deuterium or hydrogen, which require relatively high pump energies (Papayannis et al., 1990; Bösenberg et al., 1997). Over the past decade, gas-filled ~~hollow-core fibers (HCFs)~~ HCFs have emerged as an attractive alternative for nonlinear wavelength conversion~~(Debord et al., 2019a, b)~~. By guiding light in a gas-filled hollow core over long interaction lengths, HCFs enable efficient nonlinear processes at significantly reduced pulse energies, while offering compactness.

Beyond atmospheric lidar applications, ~~hollow-core fibers~~ HCFs have found widespread use in laser science and nonlinear optics (Debord et al., 2019). When filled with gases, they provide long light–matter interaction lengths enabling efficient nonlinear processes such as supercontinuum generation, ultrafast pulse compression, and Raman-based wavelength conversion at relatively low pulse energies. These capabilities have led to the emergence of the field of "gas photonics" and make gas-filled HCFs attractive candidates for compact wavelength conversion sources. ~~(Debord et al., 2019a)~~

In this context, we present the DIfferential Absorption microlidar for Boundary Layer Ozone (DIABLO), a compact ozone DIAL instrument that integrates a high repetition rate laser source, a deuterium-filled ~~hollow-core fiber~~ HCF Raman module to generate the on- and off-line UV wavelengths required for ozone DIAL measurement, and a small size optical receiver (Chafer et al., 2022). To our knowledge, this is the first demonstration of a ~~hollow-core-fiber-based~~ HCF-based Raman source fully integrated into a UV ozone DIAL microlidar and applied to atmospheric ~~boundary-layer measurements. By exploiting the high Raman gain achievable in gas-filled HCFs, DIABLO achieves efficient UV wavelength conversion at low pump energies, enabling a compact and potentially autonomous system suitable for routine operation.~~ PBL measurements.

Section 2 describes the instrument design, detailing the optical source, the receiver, and the data processing. Section 3 presents the characterization of stimulated Raman scattering in ~~hollow-core fibers~~ HCFs for different fiber lengths and gas pressures. ~~Finally,~~ Section 4 evaluates the performances of DIABLO, addressing its capability to retrieve reliable ozone profiles in the urban boundary layer. Finally, section 5 details developments still needed to turn the DIABLO prototype into an operational lidar monitoring vertical ozone variability in the planetary boundary layer and lower troposphere.

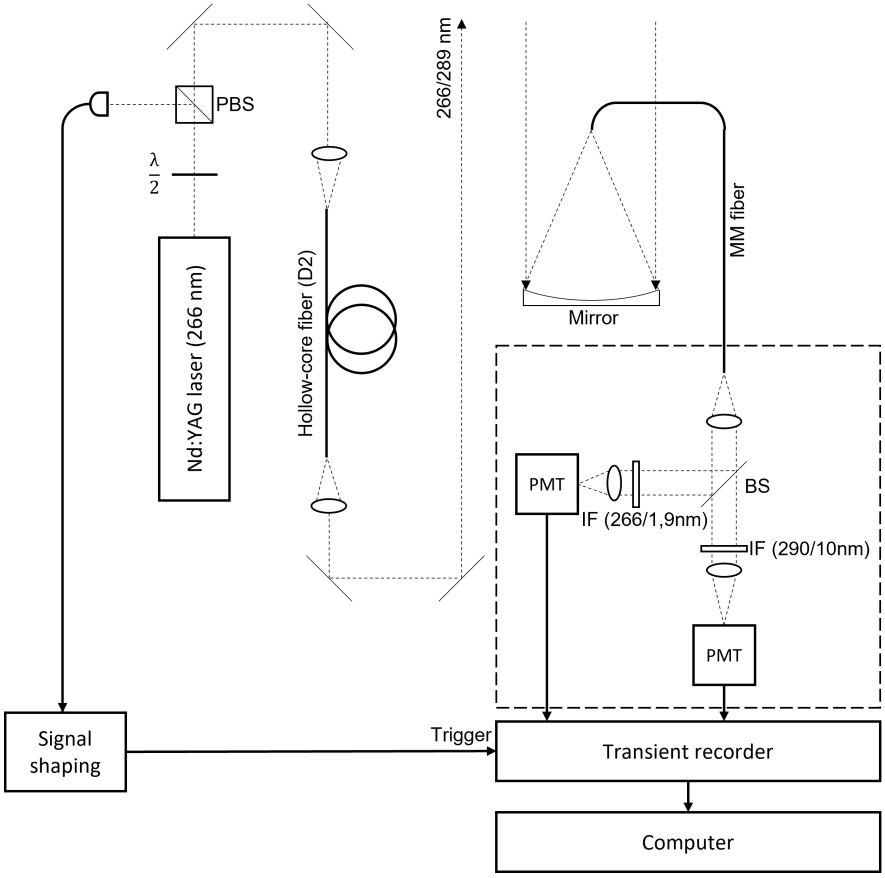


Figure 1. Schematics of the DIABLO instrument. MM stands for multimode, IF for interference filter, BS for beam splitter, PBS for polarization beam splitter, PMT for photomultiplier tube, and D2 for deuterium.

2 Instrument design

2.1 Optical source

A schematic of the ~~DIfferential Absorption microlidar for Boundary Layer Ozone (DIABLO)~~ DIABLO instrument is shown in figure 1. The DIABLO transmitter (Chafer et al., 2022) is based on a commercial diode-pumped passively Q-switched Nd:YAG laser with integrated 266 nm generation, delivering 1-ns pulses of 40 μJ at 1 kHz. The 266 nm pulse is coupled with over 70% efficiency into a ~~hollow-core fiber (HCF)~~HCF. A power-control module consisting of a half-wave plate and a polarization beam splitter is used to adjust the optical power injected into the HCF, preventing fiber damage during alignment. The rejected beam from the power-control stage is directed to a photodiode and used to trigger the lidar acquisition. ~~Hollow-core fibers~~ HCFs offer a compact and efficient alternative to conventional Raman cells for nonlinear wavelength conversion in the ultraviolet (UV) range. In these fibers, light propagates through a gas-filled hollow core surrounded by a microstructured silica cladding

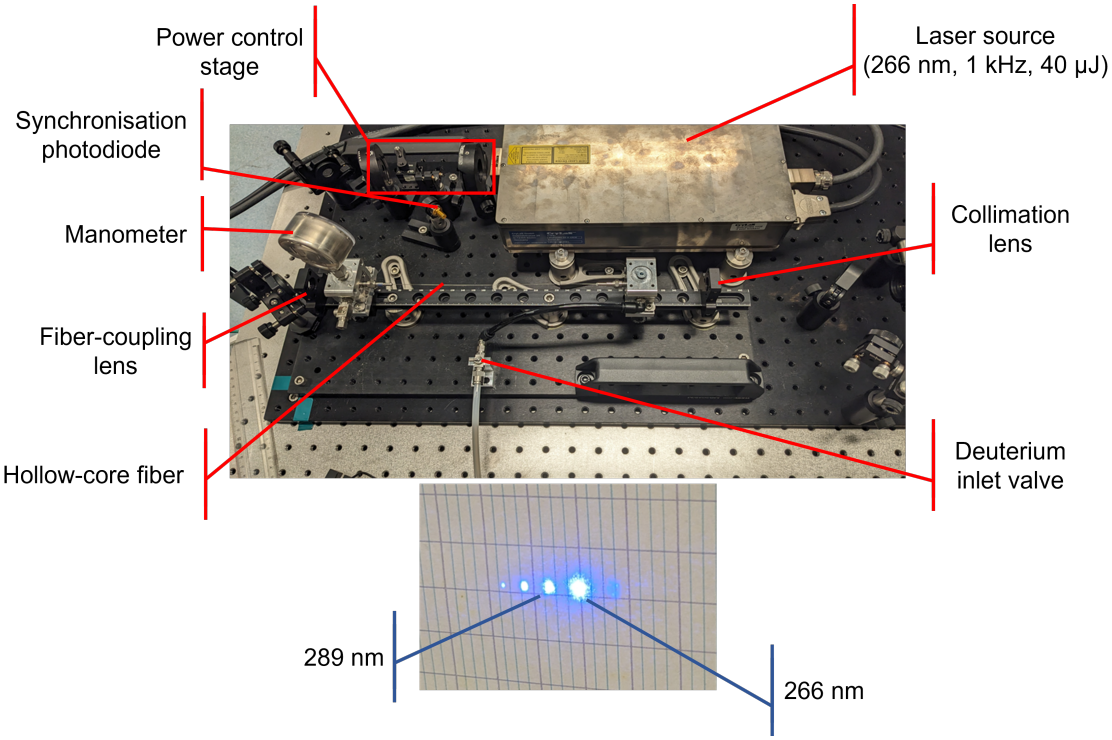


Figure 2. Picture of the optical source with identification of its main elements (top). Picture of the Raman Stokes after the HCF following wavelength separation by a prism, showing the on- and off-wavelength and the higher-order Stokes components (bottom).

that provides photonic or anti-resonant guidance. This configuration allows long interaction lengths and flexible control of the nonlinear medium through gas choice and pressure. In our system shown in figure 2, stimulated Raman scattering in a deuterium-filled HCF is used to generate the off-line wavelength required for ozone DIAL measurements. The frequency-quadrupled Nd:YAG laser at 266 nm serves as the pump, which excites coherent molecular vibrations of deuterium. Above the Raman threshold, energy is transferred from the pump to the first Stokes component at 289 nm, through a coherent scattering process that amplifies the Stokes wave along the fiber. The distribution of the energy among the pump and the 1st Raman Stokes can be tuned with the fiber length, and the gas pressure inside the HCF. Efficient coupling of the 266-nm beam into the ~~hollow-core fiber~~ HCF is challenging due to its low numerical aperture (NA ≈ 0.02), resulting in tight angular acceptance and making the system highly sensitive to alignment conditions. Using a 25-cm long HCF with a pressure of 6.5×10^5 Pa of deuterium, 1-ns pulses with an energy of 10 μJ at 266 nm and 7 μJ at 289 nm are generated, corresponding to a Raman conversion efficiency of 25% for the 266 nm and 17,5% for the 289 nm. For comparison, the existing DIAL systems (which perform SRS in a traditional Raman cell) typically report conversion efficiencies of 20% in pure Deuterium (Ancellet and Ravetta , 1998). The efficiencies obtained here with a ~~hollow-core fiber~~ HCF are therefore of the same order of magnitude as those achieved with established Raman-cell-based systems, with the additional advantage of having a more compact and integrated architecture.

The emitted beam ~~divergence is estimated below 1 mrad for both wavelengths after collimation, which is~~ divergences are estimated to be below approximately 2 mrad after collimation. However, the divergence measurement method did not accurately resolve wavelength-dependent differences. Although these estimates are smaller than the receiver full-angle field of view ~~(~~of 5 mrad~~). This ensures that the transmitted and received beams are well overlapped over the receiver field of view.~~ , they do not by themselves establish complete or identical overlap at both wavelengths.

The UV beam containing the on- and off-wavelengths is coaligned with the receiving telescope using two steering mirrors.

2.2 Receiver

The receiver consists of a compact parabolic telescope (diameter 15 cm) coupled to a fiber resulting in a 5-mrad full angle field of view. The separation between the transmitter and receiver axes is approximately 12 cm. The collected light is directed to a two-channel UV spectrometer, where a dichroic mirror separates the 266- and 289-nm wavelengths. Each arm includes a narrowband interference filter (IF) (1.9 nm at 266 nm, 10 nm at 289 nm) to minimize solar background and to avoid optical crosstalk between the two channels, followed by a flux-collector lens pair imaging the pupil onto photomultiplier tubes. The atmospheric signals are recorded by a LICEL transient recorder providing both analog and photon-counting detection for the two wavelengths. The analog channels use 12-bit digitization with a range sampling interval of 7.5 m, corresponding to a temporal sampling interval of 50 ns (20 MHz). The photon-counting signals are recorded with a range-bin spacing of 30 m.

The alignment between the transmitted laser beam and the receiver field of view is achieved using a procedure based on a 532-nm alignment laser. First, the horizontal propagation axis of the UV beam is defined using two pinhole apertures. The UV laser is then turned off and replaced by the 532-nm alignment laser, injected along the same optical path using a removable mirror. The 532-nm beam is adjusted to pass through the two pinholes separated by 100 cm, ensuring coalignment with the UV beam better than 2 mrad, and is then redirected vertically using two steering mirrors. A corner cube retroreflector is positioned above the telescope to inject the green beam into the receiver and couple it into the detection fiber. The steering mirrors are adjusted to maximize the optical power collected at the fiber output, ensuring optimal overlap between the transmitted beam and the receiver field of view. After alignment, the retroreflector and the visible laser are removed, and the UV laser is restored. A final optimisation is performed by looking at the atmospheric lidar signals. This procedure ensured coalignment of the emitted UV beam with the telescope axis.

2.3 Data processing

Ozone profiles are retrieved from the backscattered measured signals, following the standard DIAL equation (Leblanc et al., 2016a, b):

$$N_{\mathrm{O_3}} = \frac{1}{2\,\Delta\sigma_{\mathrm{O_3}}}\left[\frac{\mathrm{d}}{\mathrm{d}z}\ln\left(\frac{P_{\mathrm{off}}(z)}{P_{\mathrm{on}}(z)}\right) - \Delta\sigma_M\,N_a(z) - \Delta\alpha_P(z) + \frac{\mathrm{d}}{\mathrm{d}z}\ln\left(\frac{\beta(z,\lambda_{\mathrm{on}})}{\beta(z,\lambda_{\mathrm{off}})}\right)\right]$$

$$N_{\mathrm{O_3}} = \frac{1}{2\,\Delta\sigma_{\mathrm{O_3}}}\left[\frac{\mathrm{d}}{\mathrm{d}z}\ln\left(\frac{P_{\mathrm{off}}(z)}{P_{\mathrm{on}}(z)}\right) - \Delta\sigma_M\,N_a(z) - \Delta\alpha_P(z) + \frac{\mathrm{d}}{\mathrm{d}z}\ln\left(\frac{\beta(z,\lambda_{\mathrm{on}})}{\beta(z,\lambda_{\mathrm{off}})}\right) + \frac{\mathrm{d}}{\mathrm{d}z}\ln\left(\frac{F(z,\lambda_{\mathrm{on}})}{F(z,\lambda_{\mathrm{off}})} - \left(\sum_{\mathrm{ig}}\Delta\sigma_{\mathrm{ig}}(z)\,N_{\mathrm{ig}}(z)\right)\right)\right] \quad (1)$$

~~$\Delta\sigma_{O_3}$ is the difference of~~ Here, $\Delta\sigma_{O_3} = \sigma_{on} - \sigma_{off}$, where σ_{on} and σ_{off} are the ozone absorption cross-sections at ~~the two wavelengths (Molina et al., 1986),~~ $\lambda_{on} = 266$ nm and $\lambda_{off} = 289$ nm, respectively (Molina et al., 1986). P_{on} and P_{off} are the number of photons collected on the detectors on the "on" and "off" channels respectively. $\Delta\sigma_M$ is the difference of Rayleigh scattering cross-sections, $\Delta\alpha_P$ is the extinction differential due to particles. N_a is the air number density, β is the backscatter coefficient including both molecular and aerosol components. $F(z,\lambda)$ is the overlap factor describing the range-dependent overlap between the transmitted beam and the receiver field of view at wavelength λ. N_{ig} and $\Delta\sigma_{ig}$ are respectively the number density and the absorption cross section differential of the interfering gas ig.

Figure 3 displays an example of the ozone retrieval sequence. Figure 3(a) presents the background-subtracted and range-corrected signals (PR^2) for both wavelengths, in analog and photon-counting modes. A good agreement is observed between the two detection modes, while photon-counting signals extend the measurement range at higher altitudes due to higher sensitivity. The progressive signal attenuation with altitude is consistent with atmospheric extinction. After applying a first-derivative Savitzky–Golay filter based on a second-degree polynomial least-squares fit (Leblanc et al., 2016b) to reduce noise, these signals are then used to derive the logarithmic slopes shown in figure 3(b), from which the altitude range suitable for ozone retrieval can be identified.

Figure 3(b) presents the logarithmic slopes derived from the on- and off-line signals for both analog and photon counting signals. The altitude range suitable for ozone retrieval is defined by the region where both on- and off-line signals exhibit consistent slopes. ~~The lower limit, around~~ A conservative lower retrieval limit of 400 m ~~, is constrained by the analog signal at 266 nm due to incomplete overlap, while the~~ is adopted because the short-range logarithmic slopes exhibit a differential instrumental distortion. Geometrical sensitivity simulations indicate that wavelength-dependent overlap, resulting from differences in beam divergence combined with residual transmitter–receiver misalignment, can contribute to this distortion. No differential-overlap correction was applied to the ozone profiles presented in this study. The upper limit, slightly below 2000 m, corresponds to the altitude where the signal-to-noise ratio becomes insufficient for reliable retrieval. ~~To optimize the effective altitude range~~For each channel, a transition ~~from analog to~~ interval between analog and photon-counting data is ~~applied to the~~ selected where their logarithmic slopes exhibit consistent values. We exclude ranges affected by photon-counting saturation, where the signal is over 90% of the maximum of the counting signal, and insufficient analog signal-to-noise ratio (SNR), where the SNR is below approximately 10. Within this interval, the slopes are combined using complementary linear weights: the analog weight decreases from one to zero, while the photon-counting weight increases from zero to one. The analog slope is used below the interval and the photon-counting slope above it. For the on-line ~~signal between~~ channel, the transition extends from 1200 ~~m and 1600 m~~to 1500 m, as indicated in ~~figure~~ Fig. 3(b). This approach avoids saturation effects affecting the photon-counting signal at short ranges while taking advantage of its higher sensitivity at higher ranges.

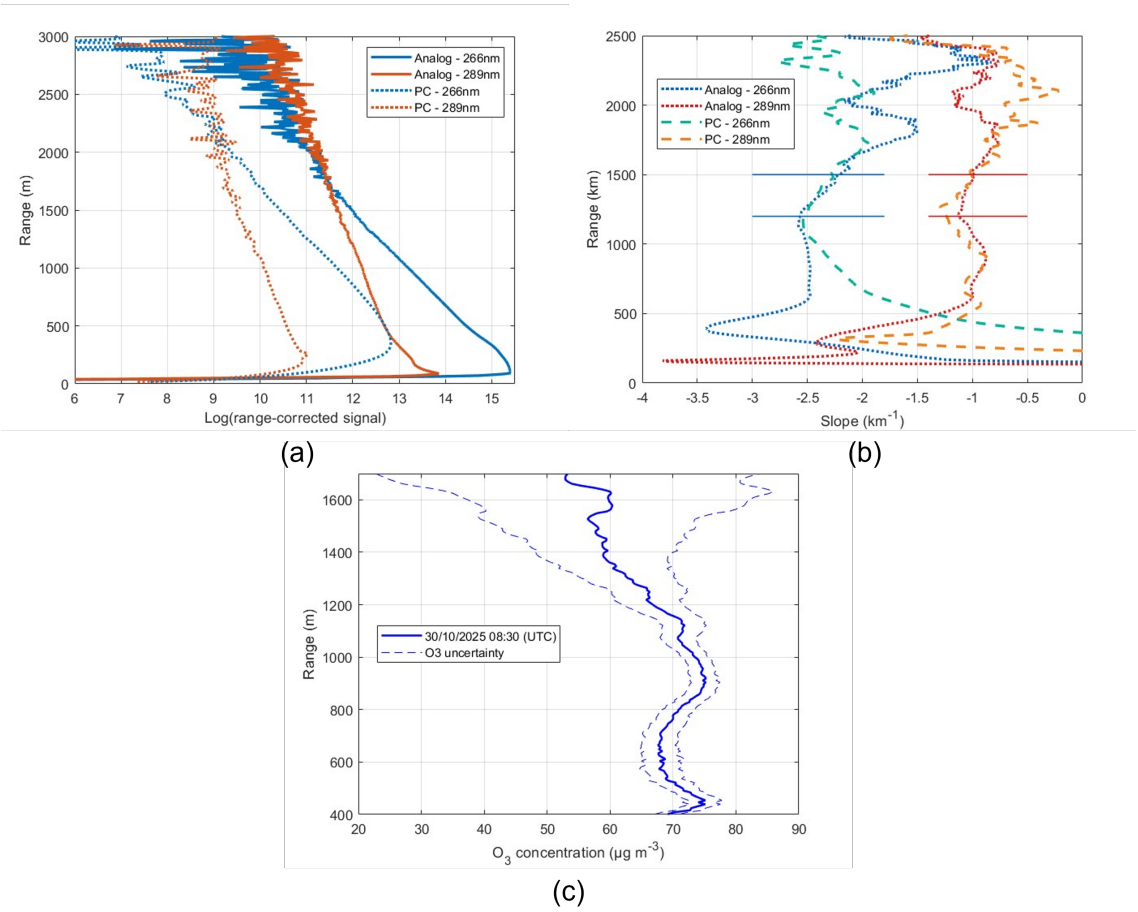


Figure 3. Example of DIAL ozone retrieval sequence. (a) Logarithm of the background and range-corrected signals in analog mode (lines) and photon-counting mode (dashed lines) for both wavelengths. (b) On- and off-line slopes of the logarithmic signals for both analog and photon counting mode. The horizontal lines indicate the gluing region. (c) Retrieved ozone concentration profile with its uncertainties due to contributions from detection noise, background subtraction, and ozone absorption cross-section uncertainty.

The logarithmic slopes derived in figure 3(b) are subsequently used to retrieve the ozone concentration profile shown in figure 3(c), following the DIAL equation. The resulting ozone profile is presented between 400 m and 1.7 km, consistently with the altitude range defined from the signal analysis. The profile presented here corresponds to the blue curve (08:30 UTC) shown in figure 6. ~~The uncertainty shown in figure 3(c) only accounts for contributions from~~

The main uncertainty sources in ozone DIAL retrievals include detection noise, background subtraction, photon-counting dead-time correction, ozone absorption cross-sections, the atmospheric temperature, pressure and interfering-gas concentration profiles used in the retrieval, aerosol interference, and differential overlap. Following Leblanc et al. (2016b), an assumed uncertainty of 2% in the individual ozone absorption cross-sections produces approximately 2% uncertainty in ozone for the 266/289 nm pair, corresponding to 1.2–1.6 $\mu g.m^{-3}$ for the concentrations measured here. The sensitivity to uncertainties in

NO_2 and SO_2 mass concentrations is approximately 0.007 and ~~ozone absorption cross-section uncertainty (Leblanc et al., 2016b) .~~ 0.045 $\mu g.m^{-3}$ of ozone per $\mu g.m^{-3}$ of the interfering gas, respectively. A 1% uncertainty in air number density used in the Rayleigh extinction correction contributes approximately 0.1–0.2% to ozone concentration uncertainty in the lower troposphere. Separately, an assumed 2% uncertainty in the individual Rayleigh scattering cross-sections yields approximately 0.1–0.3 ppbv uncertainty in ozone. O_2 absorption can be corrected using the air density profile used for the Rayleigh extinction correction. Detection noise and background-subtraction uncertainties are propagated for the profile shown in figure 3(c), whereas the dead-time correction contribution remains to be evaluated.

~~No correction for overlap or differential aerosol extinction between the two wavelengths is applied. The analysis is restricted to altitudes above the incomplete-overlap region (≈ 400 m), where the overlap function is expected to be close to unity and its impact on the retrieval is negligible. Aerosol-related effects are known to introduce uncertainties in ozone DIAL retrievals, but their magnitude strongly depends on aerosol loading and optical properties (Kuang et al., 2020). Under low aerosol conditions, such effects are generally considered to remain limited to a few percent in previous ozone lidar studies (Leblanc et al., 2016b; Wang et al., 2017). In the present case, ceilometer observations did not indicate significant aerosol loading within the PBL, suggesting that the impact of aerosols is small. The associated systematic uncertainty is therefore estimated to be on the order of 5%, although it may be significantly larger under high aerosol loading conditions. This contribution is not included in the uncertainty displayed~~Available daytime AERONET observations show AOD below 0.1 at 340 nm on the measurement days, and aerosol lidar quicklooks indicate a relatively homogeneous lower scattering layer, with a transition near 1 km and no distinct elevated aerosol layers apparent up to 2 km. The backscatter-ratio contribution is therefore expected to be smaller away from this transition, while the low observed AOD suggests limited integrated aerosol extinction. However, the gradient near 1 km may introduce a substantial local bias in the ozone retrieval up to 20%(Browell et al., 1985; Papayannis et al., 1990; Kuang et al., 2020) . No aerosol correction was applied to the ozone profiles presented in this initial demonstration, and the associated systematic contribution remains unquantified. Future processing developments will include aerosol corrections and propagation of their uncertainties as part of the complete instrument uncertainty budget required before operational deployment.

Following the NDACC definition (Leblanc et al., 2016a), the vertical resolution is derived from the full width at half maximum (FWHM) of the processing response function multiplied by the lidar sampling resolution. For the second-order Savitzky–Golay filter used here, this yields a vertical resolution of 80 m at 400 m, 225 m at 1000 m, and 520 m at 1500 m.

3 Laser source characterization

The performance of the DIABLO transmitter is primarily governed by the efficiency of the Raman wavelength conversion stage based on a gas-filled ~~hollow-core fiber~~HCF. This section presents the characterization of the Raman source in terms of output energy.

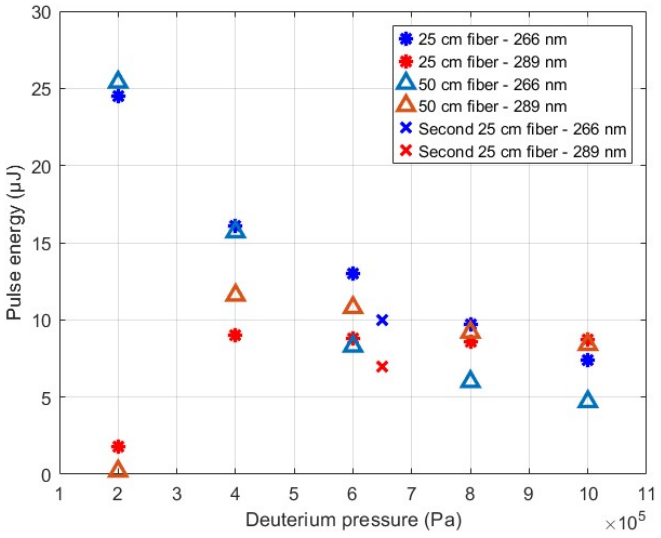


Figure 4. Pressure dependence of pulse energies at 266 nm and 289 nm in deuterium-filled ~~hollow-core fibers~~ HCFs with coupling efficiencies of 69% (25 cm) and 65% (50 cm), also showing the energy points for a second 25 cm fiber used for the LIDAR measurements presented later in the article.

3.1 Output energy and Raman conversion efficiency

Ultraviolet pump pulses at 266 nm are injected into the deuterium-filled ~~hollow-core fiber~~HCF, where stimulated Raman scattering progressively transfers energy from the pump wave to the first Stokes component at 289 nm. The balance between residual pump energy and converted Stokes energy is governed by the Raman gain, which increases with gas pressure and effective interaction length.

Figure 4 shows the evolution of the pulse energies at 266 nm and 289 nm as a function of deuterium pressure for 25 cm and 50 cm long fibers, measured after spectral separation using a prism. At low deuterium pressures, a slight decrease in the pump energy is observed, while the first Stokes signal remains weak. Between 2×10^5 Pa and 4×10^5 Pa, the pump energy decreases rapidly, accompanied by a strong increase in the Stokes energy, which reaches a maximum around 4×10^5 Pa. At higher pressures, the pump energy continues to decline, indicating ongoing energy transfer. Simultaneously, the first Stokes energy slightly decreases, as the energy is transferred to higher-order Raman Stokes components. No significant difference is observed between the two fiber lengths, indicating that increasing the propagation distance from 25 cm to 50 cm does not lead to a noticeable change in the nonlinear response. This is consistent with the observation of a multimode output beam, suggesting that the modal content is primarily governed by the input coupling conditions, which also likely lead to the excitation of higher-order spatial modes. A single-mode-like beam would be expected to improve Raman conversion efficiency through better spatial overlap between the optical beam and the gas interaction volume, as well as higher peak intensity. The circles

represent the performances obtained during the ozone measurements presented in figures 3 and 6, with 10 μJ at 266 nm and 7 μJ at 289 nm for a Deuterium pressure of 6.5×10^5 Pa.

Overall, the results presented in figure 4 clearly illustrate the strong dependence of Raman conversion on gas pressure. Low pressures result in limited energy transfer, whereas higher gas densities promote efficient conversion toward the first Stokes wavelength.

3.2 Selection of the operational configuration

The operational point selected for DIABLO and shown in figure 4 corresponds to a 25 cm fiber filled with 6.5×10^5 Pa of deuterium. Under these conditions, typical output energies of approximately 10 μJ at 266 nm and 7 μJ at 289 nm are obtained. It represents a well-balanced regime in which both wavelengths retain sufficient energy for DIAL operation, while avoiding excessive conversion toward higher-order Raman lines that would reduce useful signal power. This corresponds to an effective Raman conversion efficiency of approximately 25% for the residual pump and 17.5% for the first Stokes component, relative to the injected energy. The characterization presented in this section demonstrates that hollow-core-fiber-based Raman sources can achieve performance comparable to that of traditional Raman cells, while offering clear advantages in terms of compactness and the ability to operate with low-energy pump laser sources for microlidar applications in operational measurement networks.

During operation, a gradual decrease ~~of the deuterium pressure inside the hollow-core fiber is usually observed. This behavior is intrinsic to the use of deuterium, a light molecule with high diffusivity, and is attributed to slow~~ in deuterium pressure is observed. Possible mechanisms include leakage at connections and seals and permeation through the ~~gas connections~~materials of the gas-containing assembly (Shelby , 1977). Under typical conditions, the pressure decreases from about 6.5×10^5 Pa to 5.5×10^5 Pa over approximately one day, depending on the fiber used. Before each atmospheric ozone measurement presented here, the HCF assembly was refilled with deuterium to a pressure of 6.5×10^5 Pa. While this pressure drift did not lead to observable degradation of the ozone retrievals over the duration of the measurements presented here, it represents a limitation for long-term unattended operation. Ensuring gas pressure stability will therefore be a key aspect of future developments aimed at achieving fully autonomous microlidar operation.

The spectral content of the output beam mainly consists of the pump wavelength at 266 nm and the first Stokes component at 289 nm. Higher-order Raman components are also generated within the ~~hollow-core fiber~~HCF. However, their contribution to the total output energy remains limited, with an estimated fraction below 5% under the operating conditions used in this study.

Given their low energy and the spectral filtering implemented in the receiver, these higher-order components are not expected to contribute significantly to the detected signals or to introduce measurable bias in the ozone DIAL retrievals.

4 Instrument performance

~~Four ozone profiles are presented in figure 6~~Figure 6 presents four ozone profiles retrieved between 400 and 1700 m above ground level, corresponding to the date and integration times shown in table 1. The measurements are carried out from the QUALAIR (QUALité de l'AIR) platform, the Sorbonne University monitoring station located in the center of Paris ~~.~~

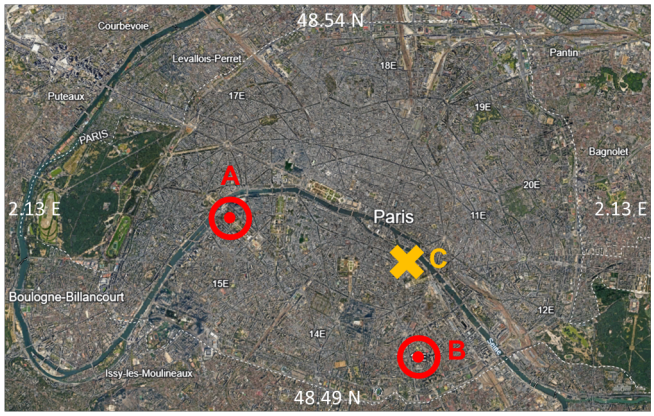


Figure 5. Google Earth map of Paris with the locations of the monitoring stations, A: Eiffel tower (300 m high), B: Paris ~~13ème~~13, C: LATMOS. Imagery and map data: © 2026 Google, Vexcel Imaging US, Inc.

Lidar profile	1	2	3	4
Date and time (UTC)	2025-10-30 08:30	2025-10-30 13:00	2025-10-30 19:00	2025-10-31 08:30
Integration time	44 min	10 min	30 min	44 min

Table 1. Dates and times of the ozone lidar measurements shown in figure 6.

~~(Klein et al., 2017, 2019; Ancellet et al., 2022). The lidar profiles extend from 400 m up to 1700 m. The second profile (red) is limited in altitude due to a shorter integration time (~~(Klein et al., 2017, 2019; Ancellet et al., 2024). Concentrations are mostly within the range of 60 to 80 $\mu g.m^{-3}$, with a maximum around 1000 m. A variability differences of approximately 10 to 20 $\mu g.m^{-3}$ is measured. The profile acquired at 13:00 UTC has a shorter vertical extent because cloud presence limited the integration time to 10 min~~) caused by cloud presence. All profiles exhibit a coherent vertical structure over the accessible altitude range~~ .

Assessing the accuracy of these profiles and their vertical structure would require independent, coincident observations from ozonesondes or another ozone lidar. Such measurements are not available for the periods presented here and are a priority for future validation. The comparisons with in situ observations and CAMS estimates allow us to examine whether the retrieved concentrations fall within a similar range and show consistent temporal variations, but do not establish the accuracy of the vertical profiles.

The surface measurements are provided by the Paris air quality network ~~(Klein et al., 2017; Ancellet et al., 2022). The Paris 13ème station, which is not directly influenced by traffic, together with the Tour Eiffel station located at~~ (Klein et al., 2017). They highlight the differences between ozone concentrations at the surface and at 300 m~~, are representative of average surface ozone in Paris. Surface ozone concentrations at the Paris 13ème stationshow strong diurnal variability ($13 - 58\,\mu g.m^{-3}$), driven by photochemical production during the day and titration and deposition processes at night. In contrast, the variability is much~~

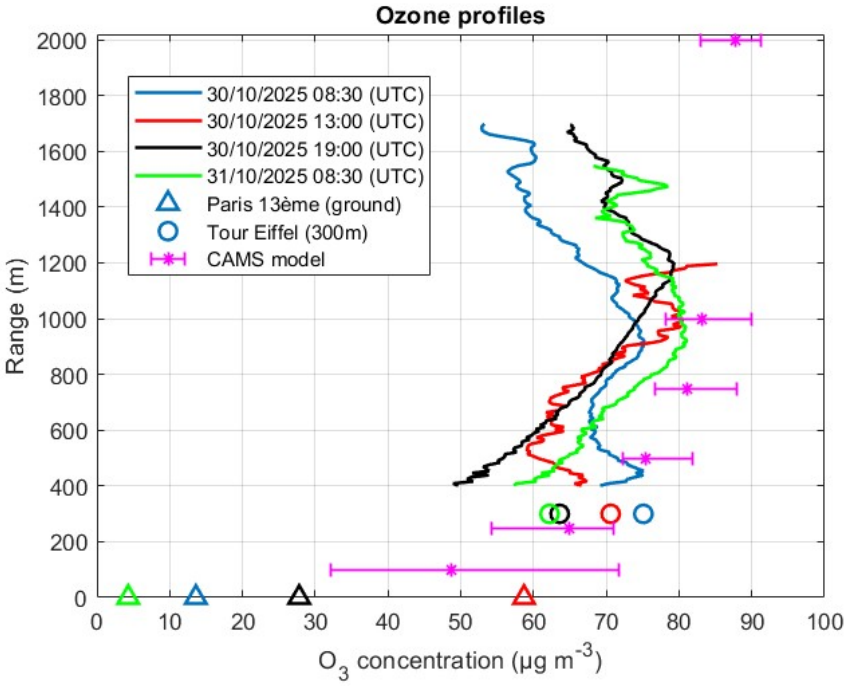


Figure 6. Comparison of ozone vertical profiles retrieved by ~~the~~ DIABLO ~~DIAL system~~ with in situ measurements and CAMS model estimates for the four measurement periods ~~(~~listed in Table ~~1)~~1. Magenta markers show the mean CAMS ozone concentration at each altitude across the four selected times corresponding to the lidar measurements. Horizontal bars show the minimum and maximum CAMS values across these times and represent temporal variability rather than model uncertainty.

~~weaker~~ . At the Paris 13 station, surface concentrations range from 13 to 58 $\mu g.m^{-3}$, whereas the Eiffel Tower observations at 300 m ~~, where the Tour Eiffel measurements range~~ remain between 62 and 75 ~~$\mu g.m^{-3}$~~. ~~The lidar retrievals reproduce this behaviour: ozone concentrations around 400 m follow the temporal evolution observed at the Tour Eiffel station, including the differences between the two morning measurements. The four consecutive acquisitions show good repeatability, with the profile measured on the following morning closely matching that of the previous day at a similar time. CAMS is the~~ $\mu g.m^{-3}$. The stronger variability at the surface is consistent with the influence of local emissions, ozone titration and deposition. The strong differences at the two heights illustrates the limitations of surface observations for monitoring ozone in the lower troposphere and motivates vertically resolved measurements. Except for the 19:00 UTC profile, the lidar concentrations near the lower retrieval limit are broadly consistent with the range observed at the Eiffel Tower. Although the measurements were carried out at different locations and heights, this agreement suggests that the retrieved concentrations are reasonable.

The Copernicus Atmosphere Monitoring Service ~~, a numerical modeling system that provides regional simulations of atmospheric composition (Marécal et al., 2015). The CAMS model value shown corresponds to the average of the ozone concentrations predicted for October 30 2025 by CAMS at 9 AM, 12 PM, 6 PM and for October 31 2025 at 9 AM, providing~~

~~a representative model estimate over the measurement period. A comparison with the model outputs shows a reasonable~~ ~~agreement between 400 m and~~ (CAMS) provides an additional estimate of the expected ozone concentration range. The regional model combines atmospheric modelling with assimilated observations (Marécal et al., 2015). Below approximately 1 km, ~~particularly in terms of the range of ozone concentrations around 1000 m~~CAMS and the lidar profiles show an increase in ozone concentration with height and similar concentration levels. Above this altitude, ~~differences between the lidar and the model become more pronounced. In the absence of independent measurements, the origin of these discrepancies cannot be assessed. As expected for UV DIAL systems, the signal-to-noise ratio decreases with altitude, leading to increased noise in the upper part of the profiles. Overall, these comparisons indicate that the temporal variability captured by the DIAL system meets the requirements for ozone profile monitoring up to 1.7 km above ground in urban environment~~their vertical structures differ: the lidar profiles generally decrease, whereas the mean CAMS concentration increases between 1 and 2 km. These differences may reflect uncertainties in the lidar retrievals, or model limitations. Independent vertical ozone observations would be needed to assess these differences, particularly above the boundary layer. CAMS is used here to provide an order of magnitude of the expected ozone concentration and its variability, without providing an independent validation of the lidar measurements.

5 Conclusions

The DIABLO prototype demonstrates the feasibility of a compact UV DIAL system dedicated to ozone profiling in the planetary boundary layer. The instrument design combines a diode-pumped, passively Q-switched laser source operating at 1 kHz with a ~~hollow-core fiber~~ HCF Raman module filled with deuterium at 6.5×10^5 Pa, enabling the generation of the required UV wavelength pair (266 ~~/~~and 289 nm) with pulse energies of approximately 10 ~~μJ~~ μJ and 7 ~~μJ~~μJ, respectively. This approach significantly reduces the ~~required~~ pump energy compared to conventional free-space Raman systems but compensates with the high repetition rate of the laser. The characterization of the stimulated Raman scattering process in the fiber shows that efficient wavelength conversion can be achieved over short interaction lengths (25 cm) and moderate gas pressures (6.5×10^5 Pa), while maintaining a balanced energy distribution between the on- and off-line wavelengths suitable for ~~DIAL retrievals~~ozone DIAL profiling. First atmospheric measurements performed in the urban environment of central Paris confirm the capability of the system to retrieve ozone profiles between approximately 400 m and ~~1.7 km~~1700 m agl., with sufficient sensitivity to capture ~~boundary-layer~~ PBL structures and their temporal variability. The ~~agreement observed with in situ measurements and CAMS model outputs supports the validity of the retrievals.~~ DIABLO concentrations near the lower retrieval limit are consistent with the concentration range measured at the Eiffel Tower. CAMS is used only to compare the order of magnitude and vertical distribution of ozone concentrations with model estimates. These initial results establish the feasibility of the proposed source architecture. Independent, coincident vertical ozone measurements are still required to assess retrieval accuracy, while extended measurements of output energy under different thermal conditions, together with mechanical stability tests, are needed to evaluate suitability for continuous autonomous operation. These results demonstrate that hollow-core-fiber-based Raman sources, combined with high repetition rate laser operation, provide a viable pathway toward compact ozone DIAL systems. ~~Overall, DIABLO contributes to bridging the gap between high-performance research-grade DIAL systems and the need~~

for more compact, deployable instruments suitable for routine air-quality monitoring. By reducing system size and required pulse energy, this approach opens new perspectives for the development of autonomous ozone profiling networksin urban environments.

Future developments will focus on improving both the instrumental design and the operational robustness of the system. In particular, the current receiver is not optimized for short-range measurements in the boundary layer. The design of a dedicated receiver with improved overlap function and reduced background noise is expected The present proof-of-concept demonstration provides a basis for developing an industrial prototype, an intermediate step towards an instrument suitable for deployment in ozone monitoring networks. This future industrial development will address three main objectives: extending the measurement range, achieving stable continuous operation, and improving measurement accuracy. Extending the usable altitude range will require a dedicated receiver design. At short range, improved collimation and transmitter–receiver alignment should reduce differential-overlap effects and enable measurements closer to the surface. At longer range, improvements to collection efficiency, spectral filtering and signal integration will be investigated to increase the signal-to-noise ratioin the lower troposphere, and to improve both the minimum and maximum measurement altitudes, thereby improving the capability to resolve near-surface ozone gradients. Another key limitation identified in the present system is the gradual decrease of deuterium pressure within the hollow-core fiber, attributed to gas permeation through the fiber connections. Although this effect does not significantly impact short-term measurements, it represents a constraint for long-term autonomous operation. Future work will therefore investigate solutions for improving gas confinement or implementing refillable fiber configurations. In parallel, efforts will be directed toward the automation of the data processing chain. The implementation of robust, real-time retrieval algorithms will be essential to enable continuous, unattended operation of the instrument. Such a work has been also achieved by the TOLNET network group in North America based on the Global Lidar Analysis Software Suite (GLASS) data processor developed by the Jet Propulsion Laboratory group (Chouza et al., 2025) Such developments are a prerequisite for integrating microlidar systems like DIABLO into operational air-quality monitoring networks. Continuous operation will require further characterization of the laser lifetime, potential fiber ageing, gas retention and the stability of the output energies at both wavelengths. Extended operating tests under different temperature conditions will be used to assess these effects and identify the necessary design changes. Improved sealing or refillable gas assemblies will be investigated to address pressure loss, while thermal regulation could be considered if the tests reveal a need for it. Improving measurement accuracy will involve optimizing the acquisition and processing for target integration times around 15 min, while accounting for the trade-off between temporal resolution, vertical resolution and measurement uncertainty. The data processing algorithm will incorporate corrections for relevant instrumental and atmospheric effects, together with propagation of their associated uncertainties, which include detector non-linearity, differential overlap, aerosol interference and absorption by other gases. Deployment alongside an aerosol lidar would provide complementary information on aerosol vertical structure and optical properties, helping to constrain aerosol corrections and quantify their uncertainty. Independent, coincident vertical ozone observations will also be required to assess retrieval accuracy before considering network deployment.

Code and data availability. The AIRPARIF network O_3 data for the Eiffel Tower station were downloaded from https://data-airparif-asso.opendata.arcgis.com/datasets/airparif-asso::2025-eiff3/explore, and those for the Paris 13 station from https://data-airparif-asso.opendata.arcgis.com/datasets/airparif-asso::2025-pa13/explore. The NetCDF files with the CAMS ENSEMBLE model hourly analysis of O_3 concentration were downloaded from https://ads.atmosphere.copernicus.eu/datasets/cams-europe-air-quality-reanalyses?tab=download.

The lidar data and its processing code are available from the authors upon request.

Author contributions. JW prepared the manuscript with contributions from all co-authors. CCF provided the infrastructure of the QUALAIR station. FR, GA, SV and VM supervised the work and validated the results. FR, GA, and JW designed the study and the experimental plan, JW and CCF carried out the experiments. JW developed the data processing code with support from GA. FD, FG, and FB provided the HCF and expertise on its implementation.

Competing interests. The authors declare that they have no conflict of interest.

Acknowledgements. This work benefited from the technical and operational support of the QUALAIR atmospheric observation platform (OSU Ecce Terra, Sorbonne University), within which the DIABLO lidar system is developed and operated. The authors also acknowledge the AIRPARIF air quality agency for providing the O3 surface data for the Paris 13ème~~me~~and Eiffel Tower stations. The European Centre for Medium-Range Weather Forecasts (ECMWF) is acknowledged for the provision of meteorological analysis data.

Financial support. This work was supported by a CIFRE PhD fellowship funded by the French National Association for Research and Technology (ANRT, grant no. 2023/1612), in partnership with CIMEL Electronique. Glophotonics supported by institutional grant from Région Nouvelle Aquitaine under OzoneFinder project.

References

Ancellet, G.and , Papayannis, A., Pelon, J., and Mégie, G.: DIAL Tropospheric Ozone Measurement Using a Nd:YAG Laser and the Raman Shifting Technique. J. Atmos. Oceanic Technol., 6, 832–839, 1989 https://doi.org/10.1175/1520-0426(1989)006<0832:DTOMUA>2.0.CO;2.

Ancellet, G. and Ravetta, F.: Compact airborne lidar for tropospheric ozone: description and field measurements, Appl. Opt.,37, 5509-5521, https://doi.org/10.1364/AO.37.005509, 1998.

Ancellet, G.and , Viatte, C., Boynard, A., Ravetta, F.: Analysis and validation of ozone variability observed by lidar during the ESCOMPTE-2001 , Pelon, J., Cailteau-Fischbach, C., Genau, P., Capo, J., Roy, A., and Nédélec, P.: Analysis of the day-to-day variability of ozone vertical profiles in the lower troposphere during the 2022 Paris ACROSS campaign, Atmos. Res. , 74, 435Chem. Phys., 24, 12963–45912983, https://doi.org/10.1016/j.atmosres.2004.10.003, 2005. 10.5194/acp-24-12963-2024, 2024.

Ancellet, G., Godin-Beekmann, S., Smit, H. G.

Bösenberg, J., Brassington, D.J., Stauffer, R.M. , Van Malderen, R., Bodichon, R., and Pazmiño, A. : Homogenization of the Observatoire de Haute Provence electrochemical concentration cell (ECC) ozonesonde data record: comparison with lidar and satellite observations, Atmos. Meas. Tech., 15, 3105–3120Simon, P.C. (eds) Instrument Development for Atmospheric Research and Monitoring. Transport and Chemical Transformation of Pollutants in the Troposphere, vol 8. Springer, Berlin, Heidelberg, https://doi.org/10.5194/amt-15-3105-2022, 2022. 10.1007/978-3-662-03405-7, 1997.

Boynard, A., Hurtmans, D., Garane, K., Goutail, F., Hadji-Lazaro, J., Koukouli, M. E., Wespes, C., Vigouroux, C., Keppens, A., Pommereau, J.-P., Pazmino, A., Balis, D., Loyola, D., Valks, P., Sussmann, R., Smale, D., Coheur, P.-F., and Clerbaux, C.: Validation of the IASI FORLI/EUMETSAT ozone products using satellite (GOME-2), ground-based (Brewer–Dobson, SAOZ, FTIR) and ozonesonde measurements, Atmos. Meas. Tech., 11, 5125–5152, https://doi.org/10.5194/amt-11-5125-2018, 2018.

Browell, E. V., Ismail, S., and Shipley, S. T.: Ultraviolet DIAL measurements of O3 profiles in regions of spatially inhomogeneous aerosols. Applied optics, 24(17), 2827–2836, https://doi.org/10.1364/ao.24.002827, 1985.

Chafer, M., Osório, J.H., Dhaybi, A., Ravetta, F., Amrani, F., Delahaye, F., Debord, B., Cailteau-Fischbach, C., Ancellet, G., Gérôme, F., and Benabid, F.: Near- and middle-ultraviolet reconfigurable Raman source using a record-low UV/visible transmission loss inhibited-coupling hollow-core fiber, Opt. Laser Technol., 147, 107678, https://doi.org/10.1016/j.optlastec.2021.107678, 2019.

Chouza, F., Leblanc, T., Wang, P., Brown, S. S., Zuraski, K., Chace, W., Womack, C. C., Peischl, J., Hair, J., Shingler, T., and Sullivan, J.: The Small Mobile Ozone Lidar (SMOL): instrument description and first results, Atmos. Meas. Tech., 18, 405–419, https://doi.org/10.5194/amt-18-405-2025, 2025.

Couillard, M. H., Schwab, M. J., Schwab, J. J., Lu, C.-H. S., Joseph, E., Stutsrim, B., Shrestha, B., Zhang, J., Knepp, T. N., and Gronoff, G. P.: Vertical Profiles of Ozone Concentrations in the Lower Troposphere Downwind of New York City During LISTOS 2018–2019, J. Geophys. Res.-Atmos., 126, e2021JD035108, https://doi.org/10.1029/2021JD035108, 2021.

Cuesta, J., Eremenko, M., Liu, X., Dufour, G., Cai, Z., Höpfner, M., von Clarmann, T., Sellitto, P., Foret, G., Gaubert, B., Beekmann, M., Orphal, J., Chance, K., Spurr, R., and Flaud, J.-M.: Satellite observation of lowermost tropospheric ozone by multispectral synergism of IASI thermal infrared and GOME-2 ultraviolet measurements over Europe, Atmos. Chem. Phys., 13, 9675–9693, https://doi.org/10.5194/acp-13-9675-2013, 2013.

Daum, P. H., Kleinman, L. I., Springston, S. R., Nunnermacker, L. J., Lee, Y.-N., Weinstein-Lloyd, J., Zheng, J., and Berkowitz, C. M.: Origin and properties of plumes of high ozone observed during the Texas 2000 Air Quality Study (TexAQS 2000), J. Geophys. Res.-Atmos., 109, D17306, https://doi.org/10.1029/2003JD004311, 2004.

Debord, B., Amrani, F., Vincetti, L., Gérôme, F., and Benabid, F.: Hollow-Core Fiber Technology: The Rising of "Gas Photonics", Fibers, 7, 16. https://doi.org/10.3390/fib7020016, 2019.

~~Debord, B.,Maurel, M.,Gerome, F., Vincetti, L., Husakou, A., and Benabid, F.: Strong nonlinear optical effects in micro-confined atmospheric air, Photon. Res. 7, 1134-1141, https://doi.org/10.1364/PRJ.7.001134, 2019.~~

Drobinski, P., Saïd, F., Ancellet, G., Arteta, J., Augustin, P., Bastin, S., Brut, A., Caccia, J., Campistron, B., Cautenet, S., Colette, A., Coll, I., Corsmeier, U., Cros, B., Dabas, A., Delbarre, H., Dufour, A., Durand, P., Guénard, V., Hasel, M., Kalthoff, N., C.Kottmeier, Lasry, F., Lemonsu, A., Lohou, F., Masson, V., Menut, L., Moppert, C., Peuch, V., Puygrenier, V., Reitebuch, O., and Vautard, R.: Regional transport and dilution during high pollution episodes in southern France: Summary of findings from the Field Experiment to Constraint Models of Atmospheric Pollution and Emissions Transport (ESCOMPTE), J. Geophys. Res., 112, D13105, https://doi.org/10.1029/2006JD007494, 2007.

Faloona, I. C., Chiao, S., Eiserloh, A. J., Alvarez, R. J., Kirgis, G., Langford, A. O., Senff, C. J., Caputi, D., Hu, A., Iraci, L. T., Yates, E. L., Marrero, J. E., Ryoo, J.-M., Conley, S., Tanrikulu, S., Xu, J., and Kuwayama, T.: The California Baseline Ozone Transport Study (CABOTS), B. Am. Meteorol. Soc., 101, E427–E445, https://doi.org/10.1175/BAMS-D-18-0302.1, 2020.

Klein, A., Ancellet, G., Ravetta, F., Thomas, J.L., and Pazmino, A.: Characterizing the seasonal cycle and vertical structure of ozone in Paris, France using four years of ground-based LIDAR measurements in the lowermost troposphere, Atmos. Environ., 167, 603-615, https://doi.org/10.1016/j.atmosenv.2017.08.016, 2017.

Klein, A., Ravetta, F., Thomas, J.L., Ancellet, G., Augustin, P., Wilson, R., Dieudonné, E., Fourmentin, M., Delbarre, H., and Pelon, J.: Influence of vertical mixing and nighttime transport on surface ozone variability in the morning in Paris and the surrounding region, Atmos. Environ., 197, 92-102, https://doi.org/10.1016/j.atmosenv.2018.10.009, 2019.

Kuang, S., Wang, B., Newchurch, M. J., Knupp, K., Tucker, P., Eloranta, E. W., Garcia, J. P., Razenkov, I., Sullivan, J. T., Berkoff, T. A., Gronoff, G., Lei, L., Senff, C. J., Langford, A. O., Leblanc, T., and Natraj, V.: Evaluation of UV aerosol retrievals from an ozone lidar, Atmos. Meas. Tech., 13, 5277–5292, https://doi.org/10.5194/amt-13-5277-2020, 2020.

Langford, A. O., Senff, C. J., Alvarez II, R. J., Aikin, K. C., Baidar, S., Bonin, T. A., Brewer, W. A., Brioude, J., Brown, S. S., Bur- ley, J. D., Caputi, D. J., Conley, S. A., Cullis, P. D., Decker, Z. C. J., Evan, S., Kirgis, G., Lin, M., Pagowski, M., Peischl, J., Petropavlovskikh, I., Pierce, R. B., Ryerson, T. B., Sandberg, S. P., Sterling, C. W., Weickmann, A. M., and Zhang, L.: The Fires, Asian, and Stratospheric Transport–Las Vegas Ozone Study (FAST-LVOS), Atmos. Chem. Phys., 22, 1707–1737, https://doi.org/10.5194/acp-22-1707-2022, 2022.

Leblanc, T., Sica, R. J., van Gijsel, J. A. E., Godin-Beekmann, S., Haefele, A., Trickl, T., Payen, G., and Gabarrot, F.: Proposed standardized definitions for vertical resolution and uncertainty in the NDACC lidar ozone and temperature algorithms – Part 1: Vertical resolution, Atmos. Meas. Tech., 9, 4029–4049, https://doi.org/10.5194/amt-9-4029-2016, 2016.

Leblanc, T., Sica, R. J., van Gijsel, J. A. E., Godin-Beekmann, S., Haefele, A., Trickl, T., Payen, G., and Liberti, G.: Proposed standardized definitions for vertical resolution and uncertainty in the NDACC lidar ozone and temperature algorithms – Part 2: Ozone DIAL uncertainty budget, Atmos. Meas. Tech., 9, 4051–4078, https://doi.org/10.5194/amt-9-4051-2016, 2016.

Liu, X., Wang, Y., Wasti, S., Li, W., Soleimanian, E., Flynn, J., Griggs, T., Alvarez, S., Sullivan, J. T., Roots, M., Twigg, L., Gronoff, G., Berkoff, T., Walter, P., Estes, M., Hair, J. W., Shingler, T., Scarino, A. J., Fenn, M., and Judd, L.: Evaluating WRF-GC v2.0 predictions

of boundary layer height and vertical ozone profile during the 2021 TRACER-AQ campaign in Houston, Texas, Geosci. Model Dev., 16, 5493–5514, https://doi.org/10.5194/gmd-16-5493-2023, 2023.

Marécal, V., Peuch, V.-H., Andersson, C., Andersson, S., Arteta, J., Beekmann, M., Benedictow, A., Bergström, R., Bessagnet, B., Cansado, A., Chéroux, F., Colette, A., Coman, A., Curier, R. L., Denier van der Gon, H. A. C., Drouin, A., Elbern, H., Emili, E., Engelen, R. J., Eskes, H. J., Foret, G., Friese, E., Gauss, M., Giannaros, C., Guth, J., Joly, M., Jaumouillé, E., Josse, B., Kadygrov, N., Kaiser, J. W., Krajsek, K., Kuenen, J., Kumar, U., Liora, N., Lopez, E., Malherbe, L., Martinez, I., Melas, D., Meleux, F., Menut, L., Moinat, P., Morales, T., Parmentier, J., Piacentini, A., Plu, M., Poupkou, A., Queguiner, S., Robertson, L., Rouïl, L., Schaap, M., Segers, A., Sofiev, M., Tarasson, L., Thomas, M., Timmermans, R., Valdebenito, Á., van Velthoven, P., van Versendaal, R., Vira, J., and Ung, A.: A regional air quality forecasting system over Europe: the MACC-II daily ensemble production, Geosci. Model Dev., 8, 2777–2813, https://doi.org/10.5194/gmd-8-2777-2015, 2015.

Molina, L. T. and Molina, M. J.: Absolute absorption cross sections of ozone in the 185- to 350-nm wavelength range, J. Geophys. Res., 91(D13), 14501–14508, https://doi.org/10.1029/JD091iD13p14501, 1986.

Monks, P. S., Archibald, A. T., Colette, A., Cooper, O., Coyle, M., Derwent, R., Fowler, D., Granier, C., Law, K. S., Mills, G. E., Stevenson, D. S., Tarasova, O., Thouret, V., von Schneidemesser, E., Sommariva, R., Wild, O., and Williams, M. L.: Tropospheric ozone and its precursors from the urban to the global scale from air quality to short-lived climate forcer, Atmos. Chem. Phys., 15, 8889–8973, https://doi.org/10.5194/acp-15-8889-2015, 2015.

Papayannis, A., Ancellet, G., Pelon, J., and Mégie, G.: Multiwavelength lidar for ozone measurements in the troposphere and the lower stratosphere. Applied optics, 29(4), 467–476, https://doi.org/10.1364/AO.29.000467, 1990.

Pelon, J. and Mégie, G.: Ozone monitoring in the troposphere and lower stratosphere: Evaluation and operation of a ground-based lidar station, J. Geophys. Res., 87, 4947–4955, https://doi.org/10.1029/JC087iC07p04947, 1982.

Ryerson, T. B., Andrews, A. E., Angevine, W. M., Bates, T. S., Brock, C. A., Cairns, B., Cohen, R. C., Cooper, O. R., de Gouw, J. A., Fehsenfeld, F. C., Ferrare, R. A., Fischer, M. L., Flagan, R. C., Goldstein, A. H., Hair, J. W., Hardesty, R. M., Hostetler, C. A., Jimenez, J. L., Langford, A. O., McCauley, E., McKeen, S. A., Molina, L. T., Nenes, A., Oltmans, S. J., Parrish, D. D., Pederson, J. R., Pierce, R. B., Prather, K., Quinn, P. K., Seinfeld, J. H., Senff, C. J., Sorooshian, A., Stutz, J., Surratt, J. D., Trainer, M., Volkamer, R., Williams, E. J., and Wofsy, S. C.: The 2010 California Research at the Nexus of Air Quality and Climate Change (CalNex) field study, J. Geophys. Res.-Atmos., 118, 5830–5866, https://doi.org/10.1002/jgrd.50331, 2013.

Senff, C. J., Alvarez II, R. J., Hardesty, R. M., Banta, R. M., and Langford, A. O.: Airborne lidar measurements of ozone flux downwind of Houston and Dallas, J. Geophys. Res.-Atmos., 115, D20307, https://doi.org/10.1029/2009JD013689, 2010.

Shelby, J. E.: Molecular diffusion and solubility of hydrogen isotopes in vitreous silica, J. Appl. Phys., 48 (8), 3387–3394, https://doi.org/10.1063/1.324180, 1977.

Strawbridge, K. B., Travis, M. S., Firanski, B. J., Brook, J. R., Staebler, R., and Leblanc, T.: A fully autonomous ozone, aerosol and nighttime water vapor lidar: a synergistic approach to profiling the atmosphere in the Canadian oil sands region, Atmos. Meas. Tech., 11, 6735–6759, https://doi.org/10.5194/amt-11-6735-2018, 2018.

Su, W., Liu, C., Hu, Q., Fan, G., Xie, Z.,Huang, X., Zhang, T., Chen, Z., Dong, Y., Ji, X., Liu, H., Wang, Z., and Liu, J.: Characterization of ozone in the lower troposphere during the 2016 G20 conference in Hangzhou, Sci Rep 7, 17368, https://doi.org/10.1038/s41598-017-17646-x, 2017.

Sullivan, J. T., Rabenhorst, S. D., Dreessen, J., McGee, T. J., Delgado, R., Twigg, L., Sumnicht, G.: Lidar observations revealing transport of O3 in the presence of a nocturnal low-level jet: Regional implications for "next-day" pollution, Atmos. Environ., 158, 160-171, https://doi.org/10.1016/j.atmosenv.2017.03.039, 2017

Uchino, O., Sakai, T., Izumi, T., Nagai, T., Morino, I., Yamazaki, A., Deushi, M., Yumimoto, K., Maki, T., Tanaka, T. Y., Akaho, T., Okumura, H., Arai, K., Nakatsuru, T., Matsunaga, T., and Yokota, T.: Lidar detection of high concentrations of ozone and aerosol transported from northeastern Asia over Saga, Japan, Atmos. Chem. Phys., 17, 1865–1879, https://doi.org/10.5194/acp-17-1865-2017, 2017.

Vautard, R., Menut, L., Beekmann, M., Chazette, P., Flamant, P. H., Gombert, D., Guédalia, D., Kley, D., Lefebvre, M.P., Martin, D., Mégie, G., Perros, P., and Toupance, G.: A synthesis of the Air Pollution Over the Paris Region (ESQUIF) field campaign, J. Geophys. Res.-Atmos., 108, 8558, https://doi.org/10.1029/2003JD003380, 2003.

Wang, L., Newchurch, M. J., Alvarez II, R. J., Berkoff, T. A., Brown, S. S., Carrion, W., De Young, R. J., Johnson, B. J., Ganoe, R., Gronoff, G., Kirgis, G., Kuang, S., Langford, A. O., Leblanc, T., McDuffie, E. E., McGee, T. J., Pliutau, D., Senff, C. J., Sullivan, J. T., Sumnicht, G., Twigg, L. W., and Weinheimer, A. J.: Quantifying TOLNet ozone lidar accuracy during the 2014 DISCOVER-AQ and FRAPPÉ campaigns, Atmos. Meas. Tech., 10, 3865–3876, https://doi.org/10.5194/amt-10-3865-2017, 2017.

Wang, X., Zhang, T., Xiang, Y., Lv, L., Fan, G., and Ou, J.: Investigation of atmospheric ozone during summer and autumn in Guangdong Province with a lidar network, Sci. Total Environ., 751, 141740, https://doi.org/10.1016/j.scitotenv.2020.141740, 2021.